



Design and characterization of the Sandia free-piston reflected shock tunnel

K. P. Lynch¹ · T. Grasser² · R. Spillers¹ · C. Downing² · K. A. Daniel¹ · E. R. Jans² · S. Kearney² · B. J. Morreale¹ · R. Wagnild¹ · J. L. Wagner¹

Received: 5 August 2022 / Accepted: 14 March 2023 / Published online: 23 May 2023
© The Author(s), under exclusive licence to Springer-Verlag GmbH Germany, part of Springer Nature 2023

Abstract

A new reflected shock tunnel capable of generating hypersonic environments at realistic flight enthalpies has been commissioned at Sandia. The tunnel uses an existing free-piston driver and shock tube coupled to a conical nozzle to accelerate the flow to approximately Mach 9. The facility design process is outlined and compared to other ground test facilities. A representative flight-enthalpy condition is designed using an in-house state-to-state solver and piston dynamics model and evaluated using quasi-1D modeling with the University of Queensland L1d code. This condition is demonstrated using canonical models and a calibration rake. A 25-cm core flow with 4.6-MJ/kg total enthalpy is achieved over an approximately 1-ms test time. The condition was refined using analysis and a heavier piston, leading to an increase in test time. A novel high-speed molecular tagging velocimetry method is applied using in situ nitric oxide to measure the freestream velocity of approximately 3016 m/s. Companion simulation data show good agreement in exit velocity, pitot pressure, and core flow size.

Keywords Shock tunnel · Velocimetry · High enthalpy

1 Introduction

Hypersonic environments exhibit a range of flow conditions and phenomena that cannot each be replicated by a single ground test facility. From the 1960s through the 1980s, Sandia operated numerous arcjet facilities, electrically heated and traditional shock tubes, and blowdown hypersonic and supersonic wind tunnels. In the late 1980s, many of these facilities were decommissioned, but the blowdown facilities remained operational. The hypersonic wind tunnel (HWT) is currently used for Mach and Reynolds number simulation in support of boundary layer transition and fluid–structure interactions studies, among others [1]. The HWT uses electrical resistance heaters to heat air or nitrogen above the condensation line in the test section (40–50 K) but is unable to reach actual flight freestream temperatures (200–300 K). There-

fore, a model placed in this cooled freestream environment experiences post-shock conditions that are different than in flight, with fewer chemical reactions, little or no surface reactions, and less radiative heat transfer. To complement the cold hypersonic flow of the HWT, a reflected shock tunnel capable of reaching higher freestream temperature has recently been constructed at Sandia.

Reflected shock tunnels and expansion tunnels are the primary facilities for generating flight-realistic environments characterized by high enthalpy and velocity. These are impulsive facilities, which use unsteady wave processes for test gas heating. This allows much higher temperatures to be generated compared to resistive or vitiated heaters, but with a limited test time on the order of milliseconds. At hypersonic speeds, these test times are sufficient for the relevant chemical, thermodynamic, and aerodynamic features to establish on a test model. Renewed interest in hypersonic flight and improvements in high-speed diagnostics have reinvigorated testing in these facilities worldwide [2–6].

The wave processes in a reflected shock tunnel are schematically illustrated in Fig. 1. A driver gas in state 4 bursts a primary diaphragm, forming a shock wave which processes the test gas, typically air, from an initial state 1 to state 2. The shock wave reflects from an end wall,

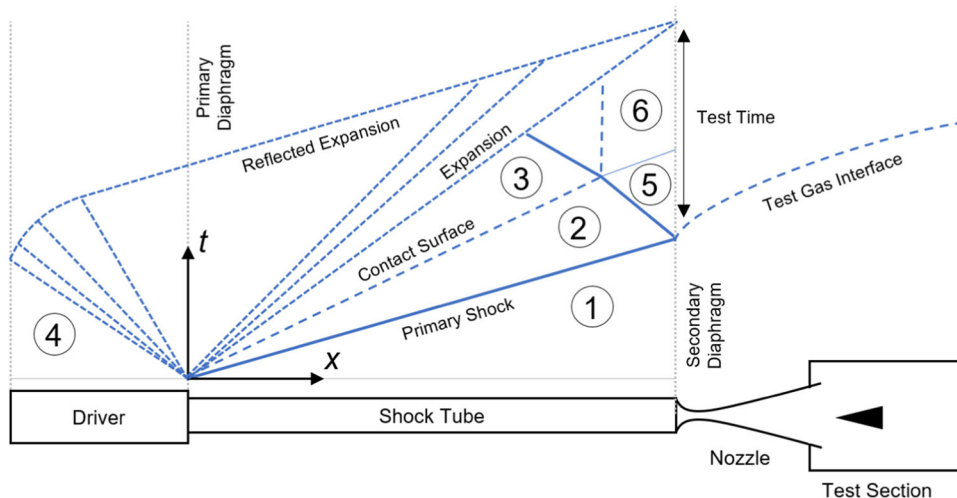
Communicated by A. Sasoh.

✉ K. P. Lynch
klynch@sandia.gov

¹ Aerosciences Department, Sandia National Laboratories, Albuquerque, NM 87123, USA

² Diagnostics Science Department, Sandia National Laboratories, Albuquerque, NM 87123, USA

Fig. 1 Reflected shock tunnel schematic and wave diagram



which further processes the state 2 gas to yield a state 5 at very high-pressure, high-temperature, and stagnant velocity. This gas bursts a secondary diaphragm, which separates the shock tube from a converging–diverging nozzle. The test section and nozzle are initially at vacuum; therefore, when the diaphragm bursts, a substantial pressure ratio is created which accelerates the test gas to hypersonic velocity.

Three factors affect the achievable test time in a reflected shock tunnel: First, the interaction between the reflected shock and the contact surface results in either an additional expansion or shock that processes the state 5 gas to state 6. Test time is maximized when this interaction is tailored such that the pressures of states 5 and 6 are equal, which also results in the contact surface being brought to rest [7]. The second factor is the arrival of either the reflected head of the expansion wave or the tail of the expansion wave, both of which originate in the driver. The expansion alters the properties of states 5 and 6; thus, delaying the arrival of these expansions increases test time. A third factor, the drainage rate of the states 5 and 6 gas into the nozzle, is dictated by the throat diameter. By accounting for these factors, test times from 1 to 10 milliseconds (ms) are typical in a reflected shock tunnel depending on the condition and geometry of the facility.

Expansion tunnels use the same or similar driver as a shock tunnel, but rather than accelerating the stagnated, doubly shocked gas using a steady expansion process, a second unsteady expansion is used for the flow acceleration. This method eliminates the need to stagnate the gas prior to expansion, which improves freestream chemistry replication by avoiding the generation of spurious chemical species (e.g., nitric oxide) and non-equilibrium thermodynamic states. This method is also capable of generating greater speeds than a shock tunnel and is the only method able to reach actual orbital reentry speeds or higher, as demonstrated by the Queensland X2 and X3 superorbital facilities [8]. This has resulted in several expansion tunnels being recently

constructed, including the CalTech Hypervelocity Expansion Tube [9], the Texas A&M hypervelocity expansion tunnel [10], the X2 and X3 facilities, and the CUBRC LENS-XX [11]. The drawback of this performance is limited test time; typical run times in an expansion tunnel are on the order of tens to hundreds of microseconds (μ s). Due to this test time limitation, it was decided to pursue a reflected shock tunnel, rather than an expansion tunnel, for this facility.

The driver method is a critical consideration in design of reflected shock tunnels, with high-performance electric, combustion, or free-piston drivers required to generate flight representative enthalpies or higher [2]. Recently at Sandia, a free-piston shock tube was constructed for studying high-temperature particle combustion [12–14] and thermochemistry of shock-heated air [15]. This driver is a similar scale to university-scale shock tunnels and was selected as the driver for our reflected shock tunnel facility.

This paper presents the current progress in bringing this facility online, including design information, photographs, and first measurements. Section 2 details the mechanical design of the facility. Section 3 describes the optical diagnostics employed. Section 4 specifies the condition design methodology and results for a flight representative case. Finally, Sect. 5 shows initial commissioning data from the optical diagnostics, tube sensors, and test section pressure rake.

2 Facility design

The Sandia HST is a small-scale free-piston facility. The mechanical design utilizes concepts of the X2 and X3 facilities. An overview rendering is shown in Fig. 2, with detail views of the nozzle, test section, and diaphragm station. The launcher is a valveless, internal plug design, with a sliding seal that decouples the recoil of the compression tube

from the reservoir section. This allows the reservoir to be connected below the compression tube to reduce the overall facility length.

The piston is 11.9 kg and machined from aluminum. The diaphragm section uses a pressure plate design similar to X3, where six 70-mm-diameter nylon buffer rods are installed to catch the piston near the end of the initial stroke for a soft landing and for protection in the event of a full-speed impact. These rods are mounted to various orifice plates, which act to secure the rods, secure the diaphragm, and control the mass flow rate of driver gas entering the shock tube for piston tuning. Orifice sizes of 8.26, 6.35, and 5.08 cm are available, with others readily machinable as needed. The pressure plate contains a PCB pressure sensor (model 113B22, 34.5 MPa range) to monitor the driver pressure. A motorized threaded capstan is used to secure the shock tube inside the compression tube.

A 336-kg inertial mass is welded near the end of the compression tube to provide additional protection for impact and overpressure events. The shock tube is assembled from multiple sections connected by Grayloc flanges. Six high-speed pressure transducers (PCB 113B24, 6.9 MPa range) are mounted throughout the length of the tube to monitor shock speeds. Two higher-range high-speed pressure transducers (PCB 113B22, 34.5 MPa range) are mounted in the compression tube and 54 mm upstream of the end-wall contraction to monitor the compressor and stagnation pressure, respectively.

A conical nozzle was chosen as the first for the facility. Conical nozzles create a freestream flow with conicity, which can complicate data analysis and interpretation [16]. However, compared to contoured nozzles, they are easier to design, produce clean, shock-free core flow across a range of enthalpies, and are shorter than a comparable contoured nozzle. The relevant design parameters are the area ratio and throat diameter. Other conical nozzles from the literature, such as the Mach 8 conical nozzle of HEG [17], were used to estimate the area ratio.

The nozzle has a throat diameter of 12.7 mm, with a circular throat cross section blended to a conical expansion of 7.9°. This more rapid expansion than nozzles used at T5 [18] and HEG was chosen due to length constraints. An area ratio of 784 was chosen based on a rough estimate of the ratio of specific heats, $\gamma = 1.3$ for the high-temperature stagnated gas. The goal was to produce a nominal Mach number of about 8 for future high-enthalpy experiments. At the lower-temperature condition herein, the exit Mach number is closer to 9, as discussed subsequently. The exit diameter of 36.5 cm is the same exit diameter as the Sandia HWT, allowing for interoperability of models between the two facilities. The secondary diaphragms are placed at the throat and made of approximately 25-micron-thick aluminum foil. These are placed in a removable stainless-steel throat insert.

The entire nozzle is connected using an interrupted-thread breech to a stagnation tube which mates to the upstream shock tube; this stagnation tube has a replaceable sleeve and contains a passthrough for a high-speed pressure transducer (PCB 113B22, 34.5 MPa range) approximately 54 mm upstream of the nozzle contraction.

The nozzle exhausts into a test section with a diameter of 0.5 m and length of 1.4 m, connected to a vertical dump tank of 98 cm diameter and 2.7 m height. The test section has four large panels able to accommodate various access; currently, a set of 25-cm-diameter 3.8-cm-thick UV fused silica window ports are installed for optical diagnostics. Models are supported by a $\pm 15^\circ$ pitch-capable vertical mount, which is anchored to a flat table on rails. This allows models to be translated into or out of the nozzle core flow region. Once at a specific location, the table is anchored to the test section using large bolts. Prior to a run, the test section and dump tank are evacuated to a high vacuum and are protected from static overpressure by a large pressure-release flange on the top of the dump tank.

A calibration rake was designed to evaluate the uniformity of pressure across the nozzle exit. The rake contains 16 high-speed pressure transducers (PCB 113B27, 690 kPa range) with 2.54-cm spacing. The sensors are mounted within a stainless-steel probe cover with four angled flow ports to prevent diaphragm fragments from damaging the sensors and shielding the sensors from any radiative heat transfer caused by flow stagnation, similar to pitot probe designs discussed in [8]. The calibration rake is mounted onto the pitch mount at zero angle-of-attack.

The major physical parameters of the facility are compared with other high-enthalpy shock tunnel facilities in Table 1. The Sandia HST is one of at least ten free-piston designs and is smaller than other national scale facilities. HST most closely compares to the recent T6 construction at Oxford University [19] and the X2 expansion tunnel at University of Queensland [20]. The small-scale of the tunnel positions the facility for conducting fundamental aerothermodynamic research with a low per-shot run and maintenance cost, housed within a facility specializing in a variety of advanced diagnostic techniques.

Construction of the Sandia HST occurred from late 2020 throughout 2021, with the first shot occurring on August 10, 2021. Photographs of the completed facility are shown in Fig. 3.

3 Optical diagnostics

3.1 Schlieren and emission imaging

Schlieren imaging was used to determine shock angles and standoff throughout the test time. Mirrors of 25.4-cm

Table 1 Comparison of reflected shock tunnel mechanical designs

Facility	Driver type*	Driver len. (m)	Driver diam. (m)	ST len. (m)	ST diam. (m)	Driver/ST len. (-)	Mach (-)	Nozzle exit diam. (m)
HYPULSE	CD	4.9	0.15	21.9	0.152	0.22	6–10	0.762
LENS-I	EH	7.6	0.28	18.3	0.203	0.4	7–18	0.91
LENS-II	EH	18.3	0.61	30.5	0.61	0.6	3–9	1.5
JF-12	CD	99.0	0.40	89	0.72	1.1	5–9	2.5
X3R	FP 280–560kg	14.0	0.50	22.0	0.20	0.64	7	0.750
HEK	FP 30kg	16.0	0.21	6.5	0.072	2.5	4.8	0.390
HELM	FP 53–150kg	21.0	0.29	8–11	0.095	2.6–1.9	9	0.684
HIEST	FP 220–780kg	42.0	0.60	17	0.180	2.4	7–13	0.8
HEG	FP 275–815kg	33.0	0.55	17	0.15	1.9	6–10	0.4–0.88
FD-21	FP 124–205kg	75.0	0.67	34	0.29	2.2	10	2.0
T4	FP 92kg	26.0	0.23	10	0.076	2.6	4–10	0.136–0.380
T5	FP 120kg	30.0	0.30	12	0.09	2.5	5.2	0.314
T6	FP 36–90kg	6.0	0.30	7.7	0.096	0.78	6–8	0.20–0.27
HST	FP 11.9kg	5.9	0.27	7.3	0.082	0.8	8	0.36

Table adapted from Stennett [21]

*FP, free piston; CD, combustion driven; EH, electrically heated

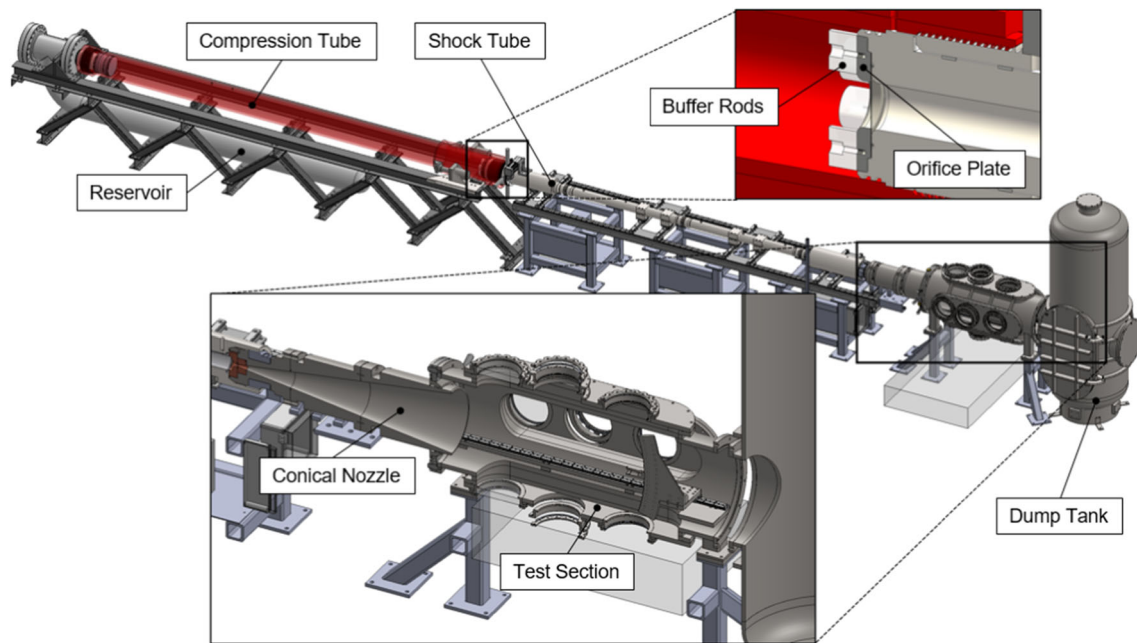


Fig. 2 Overview schematic of the HST. Translucent item under the test section represents a floating optical table

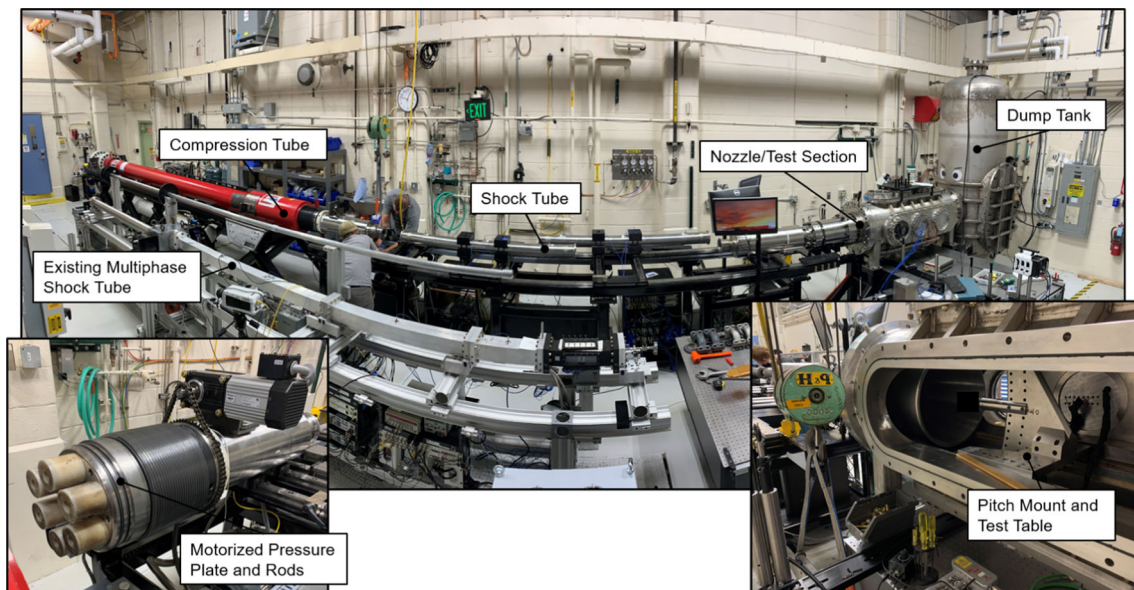


Fig. 3 Photographs of completed facility in August 2021. Panoramic photograph also shows multiphase shock tube [22]

diameter and 1.8-m focal length were placed in a Z-arrangement. A vertically oriented knife edge was placed at the collection-side focal point, and a 200-mm achromat lens was used to form the image on a Phantom v2512 monochrome camera operating at full resolution at 25 kHz. Illumination was provided by a Cavilux Smart UHS pulsed laser generating 40-ns pulses for 10 ms.

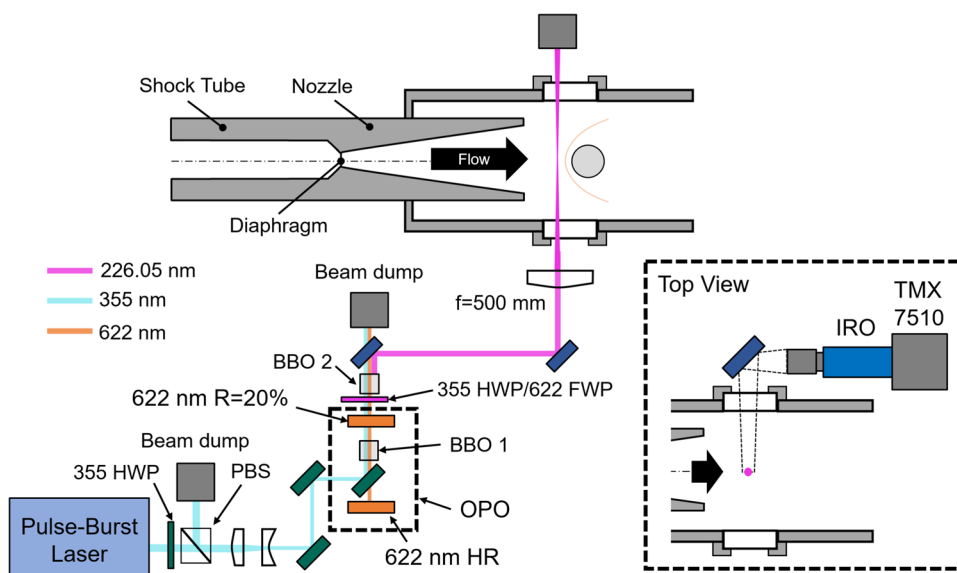
Color imaging was used to visualize the high-temperature air emission near the stagnation point. A Phantom v1212 color camera was operated at full resolution at 6 kHz with

160- μ s exposure time. A white balance was captured prior to each run for approximate color replication.

3.2 Nitric oxide velocimetry

A novel application of nitric oxide (NO) molecular tagging velocimetry (MTV) was used to characterize the velocity through the startup transient and steady test time. The high temperature of the stagnation region leads to substantial NO formation that chemically freezes due to the rapid expansion

Fig. 4 Schematic of NO MTV diagnostic:
HWP/FWP, half-/full-wave plate; PBS, polarizing beamsplitter; OPO, optical parametric oscillator; BBO, beta-barium borate; HR, high reflector



through the nozzle. Thus, the nozzle exit contains an appreciable fraction of NO (a few percent) that can be exploited for a velocity measurement. Compared to MTV schemes using, e.g., krypton or acetone, this method does not require prior seeding of the shock tube gas. Compared to femto- or picosecond laser excitation tagging (FLEET/PLEET; [23, 24]), this method is less intrusive because it deposits significantly less energy into the flow. Further, this method is compatible with high-speed pulse-burst nanosecond sources to evaluate transient behavior.

The method is schematically shown in Fig. 4. The 355-nm output of a pulse-burst Nd:YAG laser (Spectral Energies Quasi-Modo) operated at 100-kHz pulse repetition rate pumps an in-house built optical parametric oscillator (OPO) to generate 800–1100 $\mu\text{J}/\text{pulse}$. The OPO consists of a 12-mm-long type-I β -barium-borate (BBO) crystal cut at $\theta = 32.8^\circ$ and is pumped with ~ 85 mJ/pulse of the 355-nm third harmonic. The pump beam has a diameter of 6 mm and ~ 8 -ns-duration pulses. The 622-nm OPO output and the residual pump beam pass through a custom waveplate that aligns the polarizations for sum frequency mixing in a second type-I BBO crystal cut at $\theta = 59.1^\circ$. The output is tuned to 226.05 nm with a bandwidth of ~ 15 cm^{-1} to excite multiple rotational levels near the (0,0) bandhead of the NO $A^2\Sigma - X^2\Pi$ system. A 500-mm singlet lens focuses the UV laser beam to a waist region near the facility spanwise centerline, resulting in a linear region of LIF emission that is captured using a UV-sensitive image intensifier (LaVision HS-IRO S20) coupled to a high-speed Phantom TMX 7510 monochrome camera. At the low-pressure freestream conditions, the observed fluorescence lifetime is ~ 80 –100 ns, which is sufficiently long to track the motion of the emitting NO molecules at speeds of 3–4 km/s. Motion of the beam waist is tracked by repetitively sequencing the delay between

the burst-mode laser pulses and the intensifier gate from 0 to 200 ns in 50-ns increments. Therefore, a single velocity measurement is made for each cycle of 5 pulses yielding an effective repetition rate of 20 kHz. The total burst contains 100 pulses, yielding 18 velocity measurements over the 1-ms burst duration. The images for each cycle are processed using a Gaussian fitting routine to estimate the line center position, and a linear regression is fit to the positions.

4 Condition design

The HST conditions are designed using a process similar to the X3R shot design outlined in Stennett [21]. This separates the design into four steps:

- (1) Definition of the target nozzle exit condition and associated reflected shock (stagnation) condition;
- (2) Determination of the initial gas states to produce the reflected shock condition with tailoring;
- (3) Determination of reservoir fill pressure and orifice plate size to yield an overdriven piston with a soft landing using a fast-running ordinary differential equation (ODE) model;
- (4) Fine-tuning of the condition using the higher-fidelity L1d4 solver.

The first HST condition design was to replicate a high-Mach flight condition at altitude. At the time of this design, a nozzle was already fabricated with an area ratio of 784, and current facility pressure limits prevent a stagnation pressure above approximately 20.6 MPa (3000 psi). The available range of replicated altitudes was determined based on these

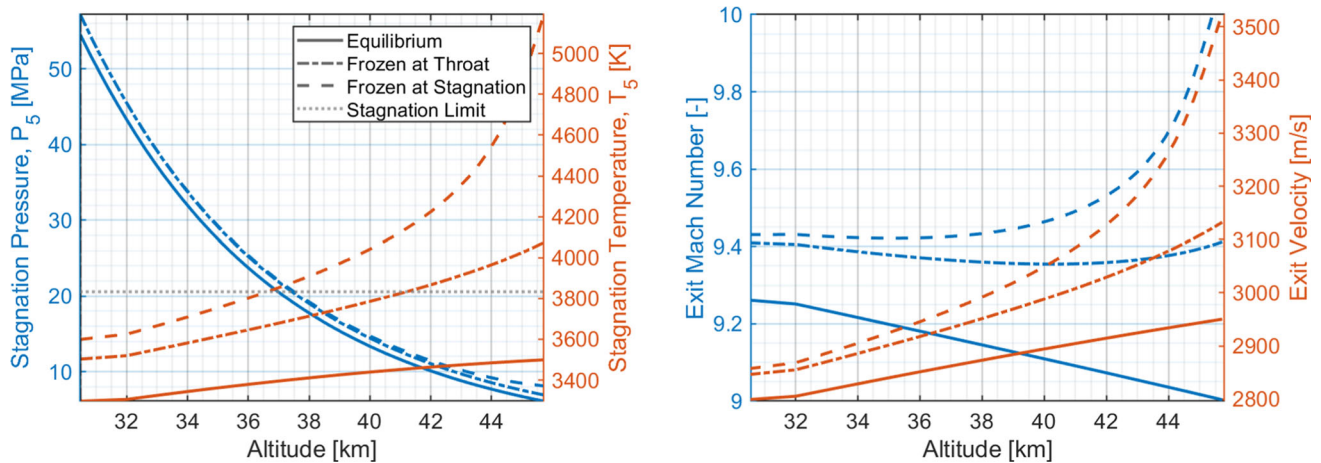


Fig. 5 Required stagnation conditions for flight replication as a function of altitude for a nozzle with area ratio 784. Left: stagnation conditions. Right: nozzle exit conditions. Dashed lines represent different levels of frozen chemistry within the nozzle

constraints. The analysis used the NASA CEA code [25] in rocket mode using air as the test gas. For a given altitude, the stagnation conditions were iterated until the outlet conditions matched the required exit conditions. The process was repeated for different locations of chemical freezing within the nozzle. This analysis is shown in Fig. 5.

The lowest altitude at which replication can be achieved is 38 km (124,800 ft). At this altitude, the standard static temperature and pressure are 246 K and 360 Pa. The predicted stagnation pressure is around 18 MPa (2610 psi), and the temperature ranges 3400–3900 K depending on the freezing state of the flow chemistry. The resulting exit velocity is between 2850 and 3000 m/s, yielding a Mach number from 9.2–9.4. For the remainder of the analysis, the flow is assumed to freeze at the throat, yielding the target stagnation condition of 18 MPa and 3700 K. Achieving pressures corresponding to lower altitude requires a higher-strength compression tube to increase the shock strength and generate higher stagnation pressure.

The required shock strength was determined using NASA CEA in shock mode by iterating shock strength and initial pressure to match the stagnation condition. For an initial shock tube temperature of 295 K, the required shock speed was 2090 m/s with initial pressure of 53 kPa. This was an initial estimate not including the effect of shock attenuation, to be discussed later.

Determining the required burst pressure and temperature is a coupled problem including the initial compressor fill pressure due to isentropic piston compression. The approach of Stennett [21] was used where these parameters are solved implicitly to yield a tailored condition where the expanded driver gas is processed by the transmitted reflected shock to an equal pressure as the stagnated gas ($P_6 = P_5$). A state-to-state solver similar to the PITOT [26] and ESTC [27] codes has been developed for this purpose, using NASA CEA

to account for high-temperature gas chemistry and steady expansion through orifice plates to determine shock strength from burst conditions.

The required burst pressure (P_4) for tailoring with an 8.26-cm (3.25-in)-diameter orifice plate was 9.6 MPa regardless of driver gas composition. A range of helium/argon fractions was analyzed to determine a suitable initial fill pressure (P_{4i}). As shown by Stennett, high fill fractions of Helium are beneficial for delaying the formation of the test-ending expansion wave for facilities with atypically short driver tubes. However, this requires a low compression ratio due to the higher performance of helium, leading to high initial Helium pressures. A 75/25% mole fraction helium/argon fill represents a suitable trade-off, with an initial fill pressure of 78 kPa, compression ratio of 18, and estimated burst temperature of 2017 K. A summary of the condition parameters is given in Table 2.

The piston motion was designed using the model of Horning [28], herein referred to as the ODE model. This consists of two ordinary differential equations describing the pre- and post-burst behavior of the piston and the compressed gases. This model was tuned, such that the piston motion would maintain forward velocity during the burst and continue compressing the driver gas as it flows into the shock tube [29]. This prevents the early formation of expansion waves in free-piston facilities, caused by the relatively short slug of compressed driver gas and rapid pressure reduction following diaphragm burst. A plot of the piston trajectory and compressor pressure from the ODE model is shown in Fig. 6. The reservoir pressure P_R was modified until the piston achieved an approximate soft landing before the end of the compression tube as defined by Itoh [30]. This occurred at approximately $P_R = 2.76$ MPa (400 psi) with the piston landing 152.4 mm (6 inches) from the diaphragm location. The piston is still moving at around 110 m/s at diaphragm

Table 2 HST flight replication condition design and measurement

	Proposed	Measured
Reservoir pressure (P_R)	2.76 MPa (400 psi)	
Test gas fill pressure (P_1)	53 kPa (7.7 psi)	
Driver gas fill pressure (P_{4i})	78 kPa (11.4 psi)	
Driver gas mole fractions	0.75 He, 0.25 Ar	
Compression ratio (λ)	18	
Burst pressure (P_4)	9.5 MPa (1390 psi)	
Burst temperature (T_4)	2017 K	
Primary diaphragm thickness	0.64 mm (0.025 in)	
Orifice plate diameter (d^*)	8.26 cm (3.25 in)	
Shock speed	2090 m/s	2100 m/s
Stagnation pressure (P_5)	18.0 MPa (2610 psi)	16.2 MPa (2350 psi)
Stagnation temperature (T_5)	3700 K	3700 K*
Freestream pressure (p_∞)	360 Pa	335 Pa*
Freestream temperature (T_∞)	243 K	235 K*
Replicated altitude	38 km (124,800 ft)	38.8 km (128,000 ft)*
Exit velocity (U_∞)	3000 m/s	3016 \pm 128 m/s

*Estimated from simulation results and/or CEA shock solution

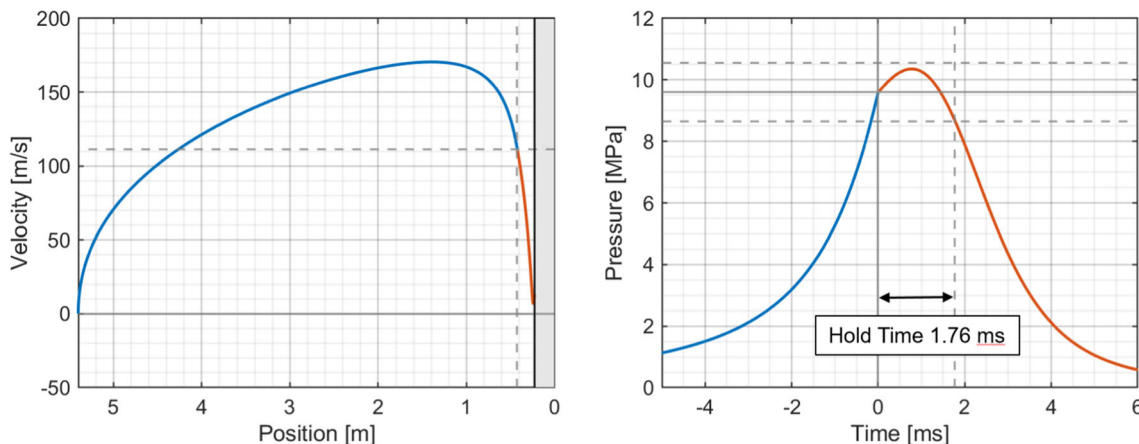


Fig. 6 Left: $x-u$ diagram of piston motion from the ODE model. Blue and orange lines represent pre- and post-burst, respectively. Dashed lines indicate burst velocity and position. Right: associated compression

pressure. Dashed lines represent $\pm 10\%$ excursion bounds from the burst pressure. The total hold time is calculated when pressure decreases -10% from burst and is shown by the vertical dashed line

burst; this overdrive of the piston leads to a sustained overpressure of $\pm 10\%$ of the nominal burst pressure for 1.8 ms.

The condition was evaluated using the University of Queensland L1d4 code [31]. This is a quasi-one-dimensional gas solver incorporating NASA CEA-based high-temperature chemistry, a pipe-flow viscosity model, and a Lagrangian grid formulation to account for moving pistons. The facility model was calibrated to account for launcher pressure losses, piston friction, and heat loss to the compression tube. A set of five blank-off tests were performed using a thick steel diaphragm (non-bursting) and an identical gas fill of 75% He/25% Ar. Pressure traces of the compressor and calibrated simulation results for two of these runs at different reservoir

pressures are shown in Fig. 7. Good agreement is obtained with L1d throughout the compression process using a single set of calibration variables for both pressures. Additionally, loss factors were introduced to the ODE model to calibrate to the blank-off data, and good agreement is obtained despite the simplicity of the flow model. Note these calibrated ODE loss factors were included in the analysis in Fig. 6.

Two later blank-off runs (181 and 182) were performed using deformable welding rods to determine the maximum extent in piston stroke and evaluate the discrepancy from the L1d model. The results of run 182 are shown in Fig. 8. The measured piston motion ends between the deformed and undeformed rod indications, corresponding to a loca-

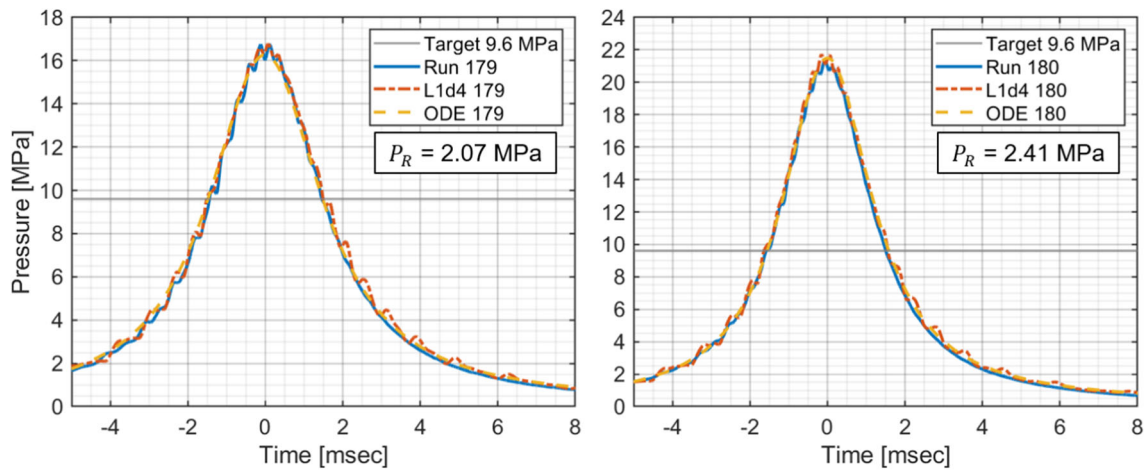


Fig. 7 Comparison of compressor pressures from blank-off runs 179 and 180. Left: reservoir pressure 2.07 MPa (300 psi). Right: 2.41 MPa (350 psi). Blue line is experimental pressure transducer data,

red dashed line is L1d simulation, and yellow dashed line is ODE model. Target burst pressure of 9.6 MPa (1390 psi) is shown for reference

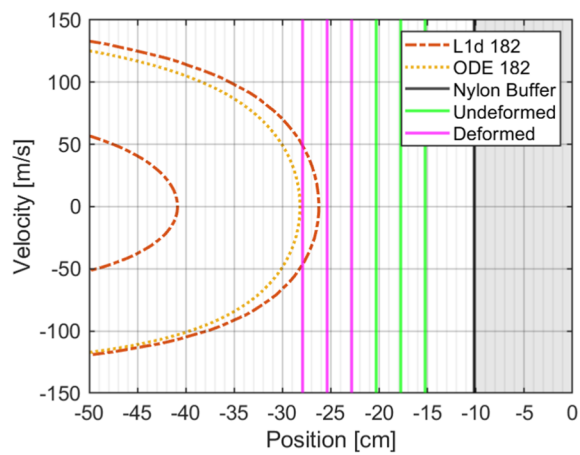
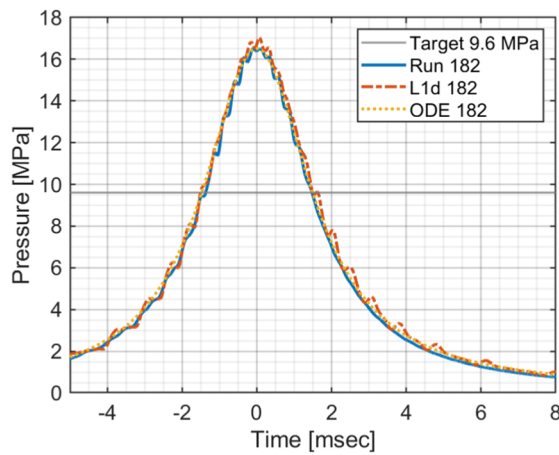
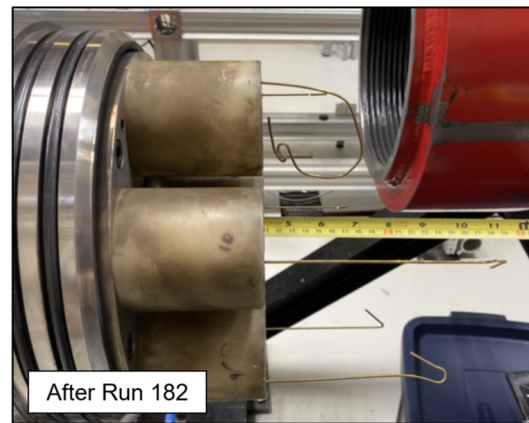
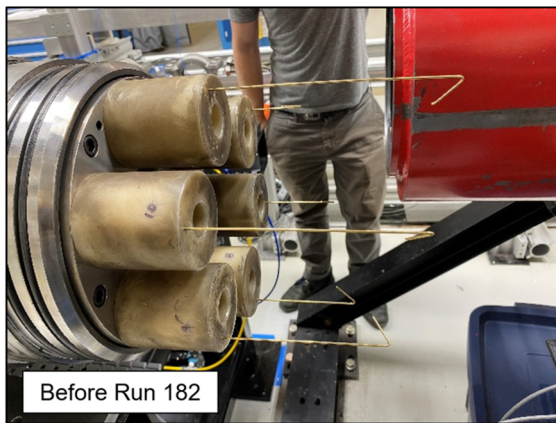


Fig. 8 Top left: photograph of undeformed weld rods installed for run 182. Top right: photograph of deformed weld rods after. Bottom left: comparison of experiment, L1d simulation, and ODE model pressure

traces. Bottom right: comparison of predicted trajectory from L1d and deformed rods (magenta), undeformed rods (green), and nylon buffer (black). Leftmost L1d trace represents the oscillating rebound of piston

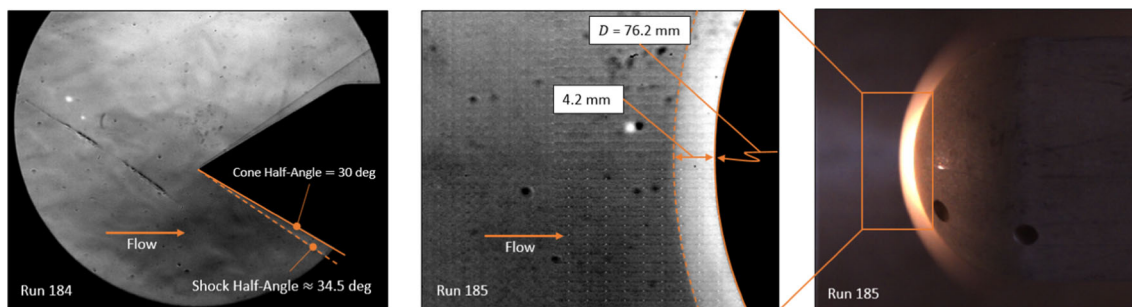


Fig. 9 Schlieren and color emission images from first shock tunnel runs with a 30° half-angle conical model (left), and blunt model (center and right). Flow is from left to right

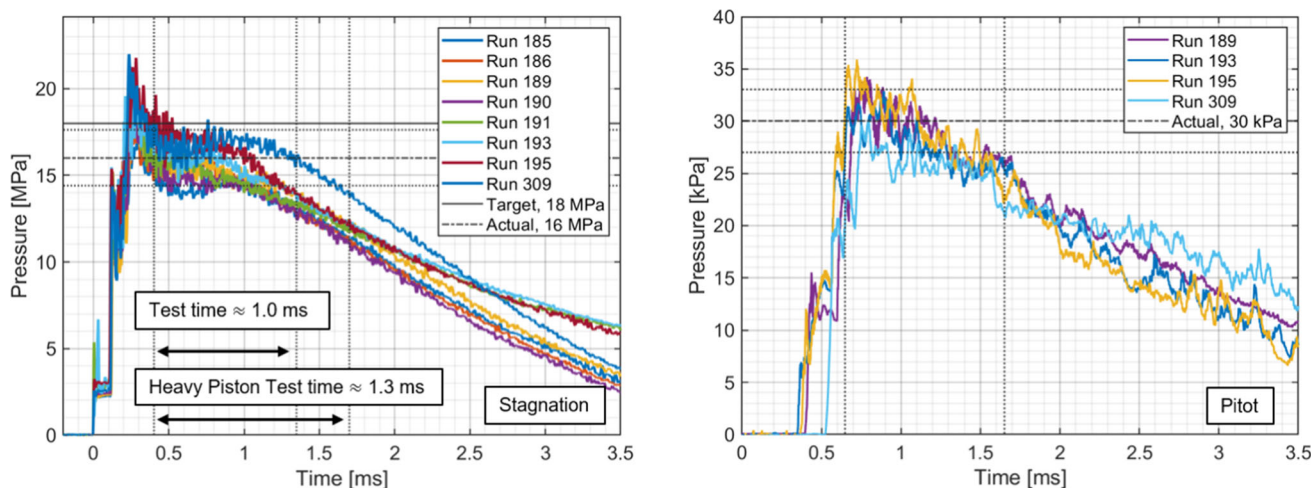


Fig. 10 Left: stagnation pressure. Right: pitot pressure along centerline. Measurements acquired simultaneously and are plotted on a consistent time axis. Test time defined as duration at $\pm 10\%$ of average pressure following tunnel start transients. Runs 191–195 used an RTV coating of the stagnation pressure sensor

tion between -20 and -23 cm. As in the previous blank-off runs, good agreement is achieved between experimental and simulated compressor pressure traces. However, both L1d and the ODE model underpredict the stroke of the piston by approximately 4–5 cm. This underprediction has been reported previously by Stennett [21], who credit it to energy loss via heat transfer to the driver tube walls. Therefore, during shot design, the maximum stroke estimated from the L1d and ODE models should be increased by this offset when choosing buffer rod lengths.

5 First shots and characterization

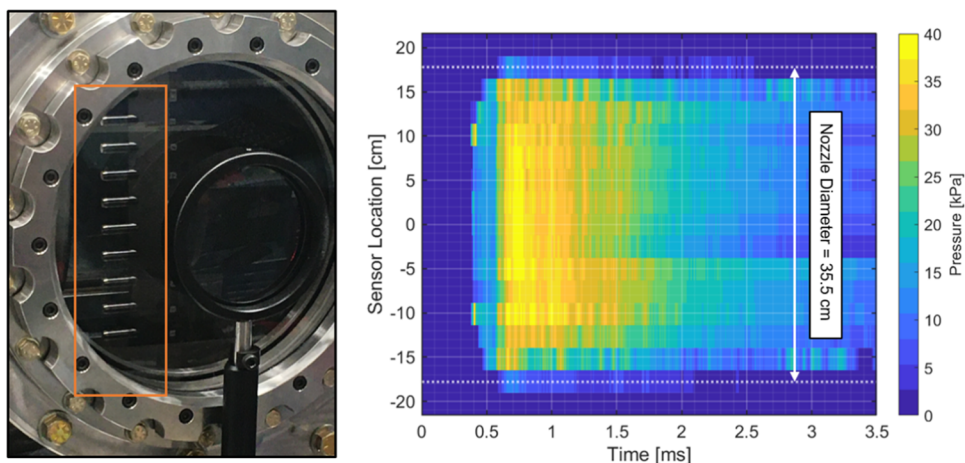
5.1 Shock standoff and pressure

A set of 14 runs were conducted based on the shot design from Sect. 3. The first 4 runs used simple canonical models to evaluate flow startup and test time. These were placed approximately 5 cm from the nozzle centerline at 0° angle of attack. Schlieren and color emission snapshots from these

experiments are shown in Fig. 9. The cone having a half-angle of 30° produces a shock angle of $\approx 34^\circ$ (left), consistent with a Mach 8–9 flow depending on the local specific heat ratio. Shock layer radiation is visualized ahead of a bluff body with color emission (right). A detached bow shock forms with a standoff of approximately 4.2 mm in the magnified schlieren view (center).

The stagnation pressures for all runs are shown in Fig. 10, left. The stagnation pressure exhibited a multistep rise, associated with the location of the sensor, which is offset from the end wall by $0.75D$. The first rise is caused by passage of the incident shock at time $t = 0$. The second rise and overshoot at 0.4 ms is due to the complex interaction between the reflected shock and the boundary layer, leading to shock bifurcation. Similar pressure profiles are observed in some, but not all, RSTs. In particular, the T6 Stalker tunnel at Oxford has shown similar behavior [19]. The pressure plateaued around 16–17 MPa, slightly lower than the target 18 MPa from the condition design, likely due to the complex shock reflection and bifurcation processes at the end wall [19].

Fig. 11 Left: photograph of calibration rake installed in the tunnel. Right: time–position contour plot of pitot pressure



After the plateau, a monotonic reduction in stagnation pressure occurred, associated with the processing of the stagnated gas by the expansion wave from the driver. Runs 191 and 193 showed different behavior caused by applying RTV on the sensor face for thermal isolation, which modified the impulse response of the sensor but removed a negative pressure bias at late times caused by thermal strains in the transducer [19]. Run 309 used a heavy piston, to be discussed in the next section. The test time is defined as the duration after the diaphragm burst where the pressure is within $\pm 10\%$ of a steady value. Approximately 1.0 ms of test time was achieved for the light piston and 1.3 ms for the heavy piston.

The corresponding centerline pitot pressures for these runs are shown in Fig. 10, right. Fewer runs were acquired with the calibration rake due to testing with other models. A less pronounced plateau in pressure occurred, but a similar $\pm 10\%$ criterion yields a similar 1.0 ms test time. Notably, a pressure oscillation was seen that is consistent between runs. At early time (0.7–1.7 ms), the oscillation frequency is around 10 kHz, and at late time (1.7–3.5 ms), the frequency reduced to around 7 kHz with some intermittency. For the heavy piston case, the increase in test time was less clear, possibly due to the end-wall geometry.

Additional details on the core flow are provided using the pitot rake (Fig. 11, left). The core flow size is evaluated using the multiple probes within the rake. A time–position contour is shown in Fig. 11, right. The two-step rise is consistent across the core flow. Uniform pressure and test time were established across a core flow region of approximately 25 cm. The core flow is processed by shear layers approximately 5 cm thick along the nozzle edge. Thus, the core flow spans about 70% of the geometric nozzle exit diameter. Also consistent across the core flow are the 7–10 kHz oscillations as illustrated from Fig. 10; however, they do not appear to be phase-aligned. This may suggest the oscillations are due to resonance within individual sensor probe covers as discussed in [8], but is not yet confirmed.

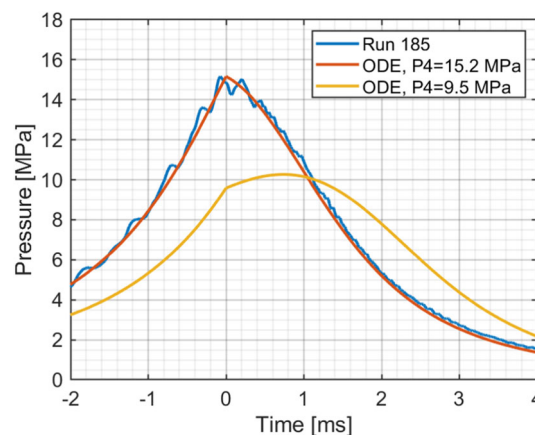


Fig. 12 Comparison between measured and modeled compressor pressure traces for different modeled burst pressures. Time 0 is the modeled burst time and the estimated burst time in the experiment

5.2 Condition improvements

The dataset from these first runs allowed the shot design to be revisited. First, the ODE and L1d models were calibrated with the actual measurements with a bursting diaphragm. A large discrepancy was observed between the modeled and actual compressor pressure as shown in Fig. 12, indicating that the burst pressure of the diaphragm when dynamically loaded was significantly higher, approximately 15.2 MPa compared to 9.6 MPa estimated from a static burst loading. Increasing the burst pressure in the models led to good agreement in the compressor pressure. Higher dynamic burst pressures compared to static loading have been noted in other facilities [21]. Additionally, the finite rupture time of the diaphragm is not accounted for in this analysis, which can influence modeling accuracy [19]. The diaphragm may begin bursting at a lower pressure, but the full burst may take additional time to develop allowing the piston to continue compression. The

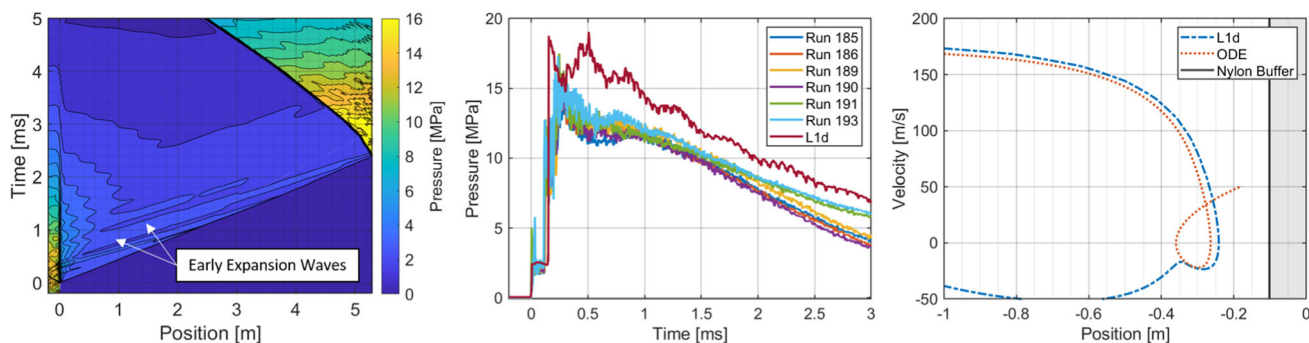


Fig. 13 L1d simulation results for the designed condition with updated burst pressure of 15.2 MPa. Left: $x-t$ diagram of pressure. Center: time trace of stagnation pressure from L1d and experiments. Right: piston dynamics from L1d and ODE solver

updated burst pressure results in rapid drainage and reduced hold time compared to the initial design.

L1d analysis using the updated burst pressure of 15.2 MPa is shown in Fig. 13. The $x-t$ diagram shows an approximately tailored condition with minimal reflected shock-contact surface interaction. However, expansion waves are formed immediately after diaphragm rupture, which propagate through the test gas and spoil the test time. This is consistent with the experimental stagnation pressure traces shown by the overlay in center.

The higher effective burst pressure affects the piston dynamics as shown in Fig. 13, right. While no experimental data on the piston position are available, both models show the piston attains zero velocity and moves backward under the influence of high pressure (a rebound motion following the nomenclature of [30]). Ideally, the piston should attain zero velocity at the moment it reaches the nylon buffer and enough gas has exhausted the driver to prevent it from being propelled backward (a soft landing).

The early expansion waves indicated that the piston hold time was too short for the increased burst pressure, or insufficiently tuned. A revised condition was designed using a 6.35-mm (2.5-in) orifice plate to reduce the flow rate of compressed gas into the shock tube. Orifice plates are effective for fine control of piston tuning but require higher burst pressures due to losses through the steady expansion at the orifice location [20]. This revised condition was implemented for runs 194–197.

The hold time can also be increased by increasing reservoir pressure and/or piston mass. The current HST reservoir is limited to approximately 4.1 MPa (500 psi), so significant increases in reservoir pressure were not possible. The piston mass of 11.9 kg was driven by the original design of the HST, which focused on generating strong incident shocks where long-duration piston overpressure was not required. Similar lightweight pistons are used in expansion tubes where the fast wave processes do not require long compressor hold times [32]. However, reflected shock tunnels do require long hold times and typically use much heavier pistons (see Table 1).

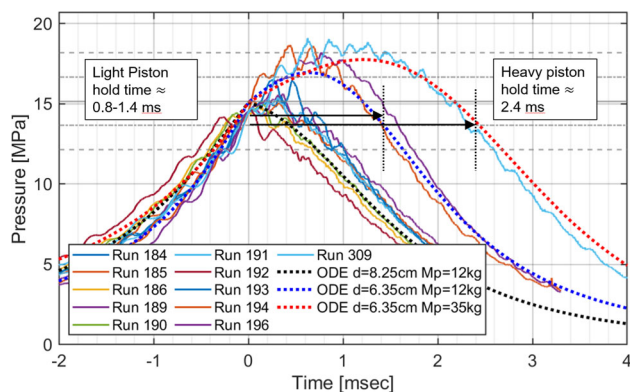


Fig. 14 Compressor pressure traces from experiments (solid lines) and comparison to ODE models (dashed lines). Horizontal gray dashed lines indicate $\pm 10\%$ and 20% variations from the estimated burst pressure of 15 MPa; d denotes the orifice plate diameter, M_p is piston mass. Time zero at crossing of estimated burst pressure

A 35-kg piston was manufactured, and a new shot design was implemented for run 309.

The compressor pressure traces for all runs are shown in Fig. 14. Overlaying the ODE model onto the original condition shows that the design had a short hold time under 1 ms. For reference, the transit time of the 2090 m/s shock wave down the 5.3 m shock tube is approximately 2.5 ms. Thus, the expansion is generated before the shock wave reflects off the end wall. The revised condition with the 11.9-kg piston and 6.35-mm orifice plate showed good agreement with the ODE model and increased the hold time to about 1.4 ms. Finally, the 35-kg piston agreed with the ODE model and increased the hold time to 2.4 ms. This increased compressor hold time resulted in a longer test time per the stagnation pressure shown in Fig. 10.

5.3 Freestream velocity

NO MTV images, fits, and velocity measurement are shown in Fig. 15. This run used the 11.9-kg piston and 6.35-cm orifice plate; however, these results apply for other configu-

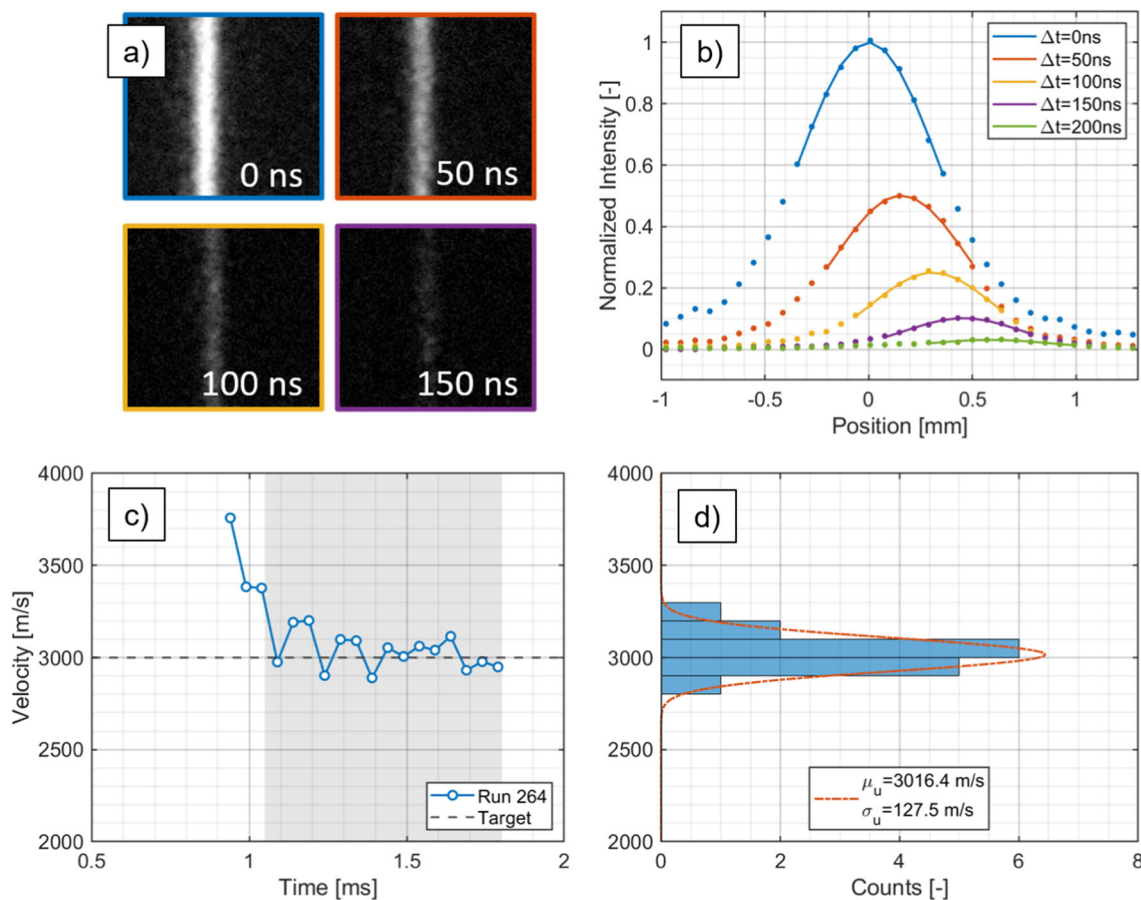


Fig. 15 NO MTV analysis: **a** Raw images of NO fluorescence with time since the initial pulse, with flow from left to right; **b** Gaussian fits (solid lines) to the image data (points); **c** time trace of velocity including

CEA-estimated exit velocity; **d** Statistical analysis of velocity measurements during the steady test time indicated by the shaded region in (c)

rations because the stagnation conditions are identical. The intensity rapidly decays across a cycle; however, a measurable displacement occurs within the decay of the LIF signal. The velocity time trace shows that the initial exit velocity exceeds the target by nearly 1 km/s because the boundary layer is not yet established on the nozzle walls resulting in a larger effective area ratio. The transient lasts around 500 μs, and the velocity reduces to the target value. The measurement uncertainty, calculated by the standard deviation of the measurements during the steady test time, is approximately 100 m/s. The uncertainty is driven primarily by the limited dynamic range due to the short fluorescence lifetime. The pulse burst duration was not long enough in this experiment to capture the end of the test. Notably, the measured velocity matches very well with the CEA predicted exit velocity assuming the chemistry is frozen at the throat location.

5.4 Comparison to modeling

The measurements were used to validate the development of a nozzle and test section flow simulation. The simulation was conducted with the Sandia Parallel Analysis and Reentry Code (SPARC) [33]. SPARC is a high-performance aerothermochemistry and fluid dynamics code being developed at Sandia. The presented simulation was run with multiblock structured grids, implicit time stepping, and with the Spalart–Allmaras RANS model to capture the growth of the boundary layer on the nozzle wall. Further, the computation used a 5-species air chemistry model and a bulk two-temperature model for vibrational non-equilibrium [34]. The nozzle was modeled axisymmetric and included the stagnation region and an extension for the test section. The initial conditions were specified as in Table 2, with the nozzle section initialized to an isentropic expansion of the stagnation condition.

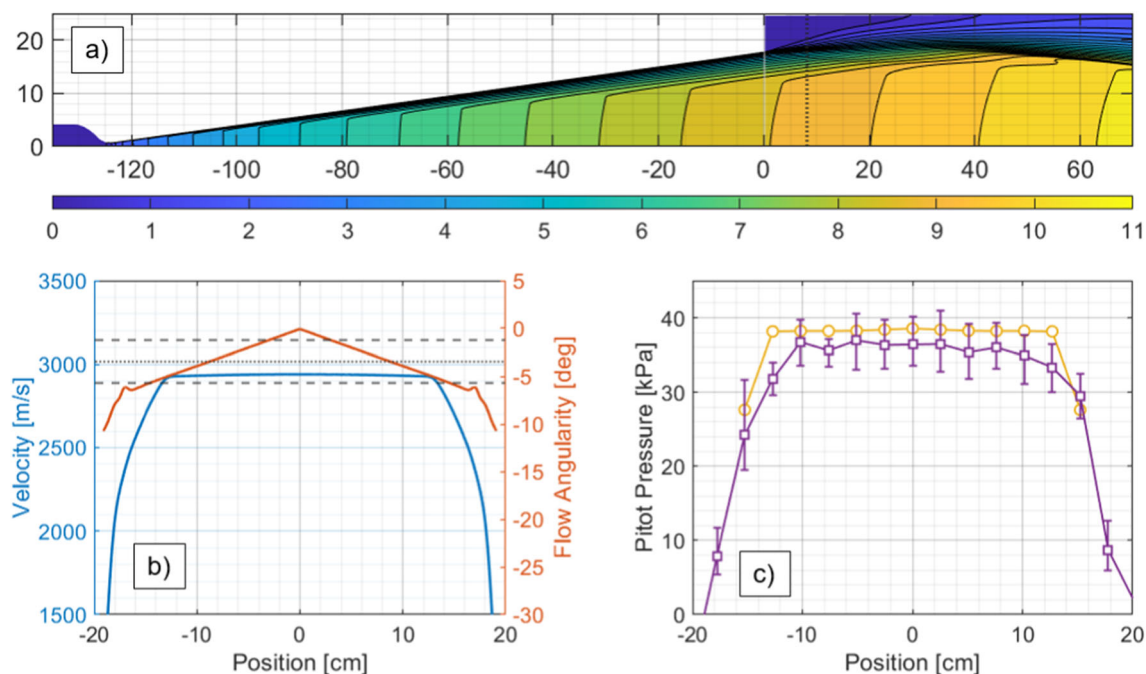


Fig. 16 Computational model and comparisons to experiment: **a** Mach number contours across top half of nozzle. Positions in cm. Dashed line at 8 cm indicates pitot rake and velocity measurement location; **b** Axial velocity and flow angularity at measurement location. Dotted and dashed lines indicate mean and uncertainty bounds of NO MTV

measurement; **c** Pitot pressure. Yellow lines and circles indicate simulated points, and purple squares and lines indicate experimental data. Error bars correspond to 5–95 percentiles of pressure within the test time interval from Fig. 10

The pitot rake was simulated using half-symmetry grids of the pitot sensor covers, with the inflow specified by a transfer from a converged nozzle/test section simulation. The half-symmetry pitot rake domain was chosen as it captures the conicity of the flow which alters the shock standoff distance for off-centerline probes.

The simulation result and comparison to measurements are shown in Fig. 16. The conical nozzle results in a continuous expansion throughout the nozzle as evidenced by the Mach contours. The residual conicity of the flow leads to additional expansion after the nozzle exit. At the measurement location, the Mach number is slightly above 9. The velocity is compared to measurement in Fig. 16b. The simulated axial velocity profile is uniform across approximately 24 cm and is slightly below the measured velocity value, but within the uncertainty bounds. Notably, the conical nozzle leads to conicity of up to approximately 5° at the edge of the core flow. The simulated pitot pressure is also approximately uniform across the core flow region and is slightly above than the measured values but also within the measurement variability. The extent of the core flow matches well to experiment, indicating the boundary layer growth is well captured by the simulation.

6 Conclusions

A new reflected shock tunnel has been commissioned at Sandia National Laboratories. The scale of the facility is amenable to fundamental research while preserving a scale suitable for instrumented models. This paper has detailed the facility design and a procedure for condition design using both low-fidelity state-to-state and piston dynamics models and higher-fidelity quasi-1D gas dynamic modeling. Calibration of the gas dynamic modeling is continuing to further fine-tune target conditions.

Initial tests show the facility can replicate approximately Mach 9 flight-enthalpy environment with demonstrated test times of approximately 1 ms, a core flow region of about 25 cm, and total enthalpy of 4.6 MJ/kg. Simple canonical models show flow features representative of a Mach 9 flow including shock layer radiation for a blunt model. A novel implementation of NO MTV measured the time-history of freestream velocity, showing a high-velocity startup followed by a steady velocity of 3.0 ± 0.1 km/s during the test time. This velocimetry method may be useful in other shock tunnel facilities where NO naturally forms in the stagnation region and freezes in the nozzle expansion. A CFD model of the noz-

zle flow was developed and compared to measured velocity and pitot pressure. Good agreement in velocity and core flow size was obtained.

Analysis of the facility performance indicates improvements to the test time were achievable by delaying the formation of expansion waves emanating from the driver. An improvement was achieved using variable diameter orifice plates and a new heavier piston.

Acknowledgements The authors thank Paul Farias for his extensive help in the mechanical design of the nozzle section. The authors also thank the staff and students at the Center for Hypersonics at the University of Queensland for numerous helpful discussions on free-piston driver operation and condition design. Sandia National Laboratories is a multimission laboratory managed and operated by National Technology & Engineering Solutions of Sandia, LLC, a wholly owned subsidiary of Honeywell International Inc., for the U.S. Department of Energy's National Nuclear Security Administration under contract DE-NA0003525. This paper describes objective technical results and analysis. Any subjective views or opinions that might be expressed in the paper do not necessarily represent the views of the U.S. Department of Energy or the United States Government.

Funding This work was funded by the U.S. Department of Energy's National Nuclear Security Administration.

Data availability The datasets generated during and/or analyzed during the current study are available from the corresponding author on reasonable request.

Declarations

Conflict of interest The authors have no competing interests to declare that are relevant to the content of this article.

References

- Beresh, S.J., Casper, K.M., Wagner, J.L., Henfling, J.F., Spillers, R.W., Pruett, B.O.M.: Modernization of Sandia's hypersonic wind tunnel. 53rd AIAA Aerospace Sciences Meeting, Kissimmee, FL, AIAA Paper 2015-1338 (2015). <https://doi.org/10.2514/6.2015-1338>
- Gu, S., Olivier, H.: Capabilities and limitations of existing hypersonic facilities. *Prog. Aerospace Sci.* **113**, 100607 (2020). <https://doi.org/10.1016/j.paerosci.2020.100607>
- Lewis, S.W., Morgan, R.G., McIntyre, T.J., Alba, C.R., Greendyke, R.B.: Expansion tunnel experiments of earth reentry flow with surface ablation. *J. Spacecraft Rockets* **53**, 887–899 (2016). <https://doi.org/10.2514/1.A33267>
- Laurence, S.J., Butler, C.S., Martinez Schramm, J., Hannemann, K.: Force and moment measurements on a free-flying capsule in a shock tunnel. *J. Spacecraft Rockets* **55**, 403–414 (2018). <https://doi.org/10.2514/1.A33820>
- Girard, J.J., Finch, P.M., Strand, C.L., Hanson, R.K., Yu, W.M., Austin, J.M., Hornung, H.G.: Measurements of reflected shock tunnel freestream nitric oxide temperatures and partial pressure. *AIAA J.* **59**, 5266–5275 (2021). <https://doi.org/10.2514/1.J060596>
- Shekhtman, D., Yu, W., Mustafa, M.A., Parziale, N.J., Austin, J.M.: Freestream velocity-profile measurement in a large-scale, high-enthalpy reflected shock tunnel. *Exp. Fluids* **62**, 1–13 (2021). <https://doi.org/10.1007/s00348-021-03207-6>
- Wittliff, C.E., Wilson, M.R., Hertzberg, A.: The tailored-interface hypersonic shock tunnel. *J. Aerospace Sci.* **26**, 219–228 (1959). <https://doi.org/10.2514/8.8016>
- Gildfind, D.E., Morgan, R.G., Jacobs, P.A.: Expansion tubes in Australia. In: Igra, O., Seiler, F. (eds.) *Experimental Methods of Shock Wave Research*, pp. 399–431. Springer, Berlin (2016). https://doi.org/10.1007/978-3-319-23745-9_13
- Dufrene, A., Sharma, M., Austin, J.M.: Design and characterization of a hypervelocity expansion tube facility. *J. Propuls. Power* **23**, 1185–1193 (2007). <https://doi.org/10.2514/1.30349>
- Dean, T., Blair, T., Roberts, M., Limbach, C., Bowersox, R.D.: On the initial characterization of a large-scale hypervelocity expansion tunnel. *AIAA SciTech 2022 Forum*, San Diego, CA, AIAA Paper 2022-1602 (2022). <https://doi.org/10.2514/6.2022-1602>
- MacLean, M., Holden, M.S., Dufrene, A.: Measurements of real gas effects on regions of laminar shock wave/boundary layer interaction in hypervelocity flows. 21st AIAA Computational Fluid Dynamics Conference, San Diego, CA, AIAA Paper 2013-2837 (2013). <https://doi.org/10.2514/6.2013-2837>
- Petter, S.J., Lynch, K.P., Farias, P., Spitzer, S., Grasser, T., Wagner, J.L.: Early experiments on shock-particle interactions in the high-temperature shock tube. *AIAA Scitech 2020*, Orlando, FL, AIAA Paper 2020-0622 (2020). <https://doi.org/10.2514/6.2020-0622>
- Lynch, K.P., Wagner, J.L.: A free-piston driven shock tube for generating extreme aerodynamic environments. *AIAA Scitech 2019*, San Diego, CA, AIAA Paper 2019-1942 (2019). <https://doi.org/10.2514/6.2019-1942>
- Daniel, K.A., Murzyn, C.M., Allen, D.J., Lynch, K.P., Downing, C.R., Wagner, J.L.: Coaxial laser absorption and optical emission spectroscopy of high-pressure aluminum monoxide. *Opt. Lett.* **47**, 2350–2353 (2022). <https://doi.org/10.1364/OL.456342>
- Winters, C., Haller, T., Kearney, S., Varghese, P., Lynch, K., Daniel, K., Wagner, J.: Pulse-burst spontaneous Raman thermometry of unsteady wave phenomena in a shock tube. *Opt. Lett.* **46**, 2160–2163 (2021). <https://doi.org/10.1364/OL.420484>
- Hornung, H.G.: Effect of conical free stream on shock stand-off distance. *AIAA J.* **57**, 4115–4116 (2019). <https://doi.org/10.2514/1.J058385>
- Hannemann, K., Schramm, J.M., Wagner, A., Camillo, G.P.: The high enthalpy shock tunnel Göttingen of the German Aerospace Center (DLR). *J. Large-Scale Res. Facil.* **4**, A133 (2018). <https://doi.org/10.17815/jlsrf-4-168>
- Marineau, E.C., Hornung, H.G.: Heat flux calibration of T5 hypervelocity shock tunnel conical nozzle in air. *AIAA SciTech*, Orlando, FL, AIAA Paper 2009-1158 (2009). <https://doi.org/10.2514/6.2009-1158>
- Collen, P., Doherty, L.J., Subiah, S.D., Sopek, T., Jahn, I., Gildfind, D., Penty Geraets, R., Gollan, R., Hambidge, C., Morgan, R., McGilvray, M.: Development and commissioning of the T6 Stalker Tunnel. *Exp. Fluids* **62**, 1–24 (2021). <https://doi.org/10.1007/s00348-021-03298-1>
- Gildfind, D.E., James, C.M., Morgan, R.G.: Free-piston driver performance characterization using experimental shock speeds through helium. *Shock Waves* **25**, 169–176 (2015). <https://doi.org/10.1007/s00193-015-0553-8>
- Stennett, S.J.: Development of an extended test time operating mode for a large reflected shock tunnel facility. Ph.D. Dissertation, University of Queensland (2020)
- Wagner, J.L., Beresh, S.J., Kearney, S.P., Trott, W.M., Castaneda, J.N., Pruett, B.O., Baer, M.R.: A multiphase shock tube for shock wave interactions with dense particle fields. *Exp. Fluids* **52**, 1507–1517 (2012). <https://doi.org/10.1007/s00348-012-1272-x>
- Michael, J.B., Edwards, M.R., Dogariu, A., Miles, R.B.: Femtosecond laser electronic excitation tagging for quantitative velocity

- imaging in air. *Appl. Opt.* **50**, 5158–5162 (2011). <https://doi.org/10.1364/AO.50.005158>
24. Jiang, N., Mance, J.G., Slipchenko, M.N., Felver, J.J., Stauffer, H.U., Yi, T., Danehy, P.M., Roy, S.: Seedless velocimetry at 100 kHz with picosecond-laser electronic-excitation tagging. *Opt. Lett.* **42**, 239–242 (2017). <https://doi.org/10.1364/OL.42.000239>
 25. McBride, B.J.: Computer program for calculation of complex chemical equilibrium compositions and applications. NASA Lewis Research Center (1996)
 26. James, C.M., Gildfind, D.E., Lewis, S.W., Morgan, R.G., Zander, F.: Implementation of a state-to-state analytical framework for the calculation of expansion tube flow properties. *Shock Waves* **28**, 349–377 (2018). <https://doi.org/10.1007/s00193-017-0763-3>
 27. McIntosh, M.K.: A computer program for the numerical calculation of equilibrium and perfect gas conditions in shock tunnels. Australian Defence Scientific Service (1969)
 28. Hornung, H.G.: The piston motion in a free-piston driver for shock tubes and tunnels. GALCIT FM 88-1 (1988)
 29. Stalker, R.J.: A study of the free-piston shock tunnel. *AIAA J.* **5**, 2160–2165 (1967). <https://doi.org/10.2514/3.4402>
 30. Itoh, K., Ueda, S., Komuro, T., Sato, K., Takahashi, M., Miyajima, H., Tanno, H., Muramoto, H.: Improvement of a free piston driver for a high-enthalpy shock tunnel. *Shock Waves* **8**, 215–233 (1998). <https://doi.org/10.1007/s001930050115>
 31. Jacobs, P.A.: Shock tube modelling with L1d. University of Queensland Research Report 13/98 (1998)
 32. Gildfind, D.E., Morgan, R.G., McGilvray, M., Jacobs, P.A., Stalker, R.J., Eichmann, T.N.: Free-piston driver optimisation for simulation of high Mach number scramjet flow conditions. *Shock Waves* **21**, 559–572 (2011). <https://doi.org/10.1007/s00193-011-0336-9>
 33. Howard, M., Bradley, A., Bova, S.W., Overfelt, J., Wagnild, R., Dinzl, D., Hoemmen, M., Klinvex, A.: Towards performance portability in a compressible CFD code. 23rd AIAA Computational Fluid Dynamics Conference, Denver, CO, AIAA Paper 2017-4407 (2017). <https://doi.org/10.2514/6.2017-4407>
 34. Park, C.: Nonequilibrium Hypersonic Aerodynamics. Wiley Interscience, New York (1990)

Publisher's Note Springer Nature remains neutral with regard to jurisdictional claims in published maps and institutional affiliations.

Springer Nature or its licensor (e.g. a society or other partner) holds exclusive rights to this article under a publishing agreement with the author(s) or other rightsholder(s); author self-archiving of the accepted manuscript version of this article is solely governed by the terms of such publishing agreement and applicable law.